

Algorithms for Non-Negative Matrix Factorization on Noisy Data With Negative Values

Dylan Green and Stephen Bailey

Abstract—Non-negative matrix factorization (NMF) is a dimensionality reduction technique that has shown promise for analyzing noisy data, especially astronomical data. For these datasets, the observed data may contain negative values due to noise even when the true underlying physical signal is strictly positive. Prior NMF work has not treated negative data in a statistically consistent manner, which becomes problematic for low signal-to-noise data with many negative values. In this paper we present two algorithms, Shift-NMF and Nearly-NMF, that can handle both the noisiness of the input data and also any introduced negativity. Both of these algorithms use the negative data space without clipping, and correctly recover non-negative signals without any introduced positive offset that occurs when clipping negative data. We demonstrate this numerically on both simple and more realistic examples, and prove that both algorithms have monotonically decreasing update rules.

Index Terms—Non-negative matrix factorization (NMF), dimension reduction, noisy data, weighted NMF, negative data

I. INTRODUCTION

NON-NEGATIVE matrix factorization (NMF) [1] is a powerful matrix factorization method that has gained significant traction as a dimensionality reduction technique. The NMF specification is, broadly speaking, to fit coefficients \mathbf{H} and templates \mathbf{W} to the (possibly noisy) data \mathbf{X} such that

$$\mathbf{X} \approx \mathbf{WH}, \quad (1)$$

with the constraints $\mathbf{X}, \mathbf{W}, \mathbf{H} \in \mathbb{R}_+$, i.e. all values in all matrices are non-negative. In this formalism, \mathbf{X} is a $d \times n$ matrix of d -dimensional data with each of the n individual data vectors on the columns of \mathbf{X} . \mathbf{W} is therefore $d \times q$ and \mathbf{H} is $q \times n$ where q is the desired number of templates to fit. Approximating \mathbf{X} necessitates defining a measure of closeness between the reconstruction and the original dataset. Here we are concerned with the Euclidean norm, which allows us to cast the problem as minimizing the objective function

$$\chi^2 = \|\mathbf{X} - \mathbf{WH}\|^2 \quad (2)$$

Manuscript submitted November 2, 2023. The work of Dylan Green was supported by the U.S. Department of Energy (DOE), Office of Science, Office of Workforce Development for Teachers and Scientists, Office of Science Graduate Student Research (SCGSR) program. The SCGSR program is administered by the Oak Ridge Institute for Science and Education for the DOE under contract number DE-SC0014664. Stephen Bailey is supported by the U.S. DOE, Office of Science, Office of High-Energy Physics, under Contract No. DE-AC02-05CH11231. This work used the National Energy Research Scientific Computing Center (NERSC), a DOE Office of Science User Facility under the same contract. (Corresponding author: Dylan Green)

Dylan Green is with the Department of Physics and Astronomy, University of California Irvine, Irvine, CA 92697 (email: dylanag@uci.edu)

Stephen Bailey is with Lawrence Berkeley National Laboratory, Berkeley, CA 94720 (email: StephenBailey@lbl.gov)

with the aforementioned constraints. A common method for solving this matrix optimization problem is to use multiplicative iterative update rules, such as those originally derived by Lee and Seung [2].

The applications for NMF as a data reduction technique are broad, and cover a variety of fields, for example geophysics [3], biology [4], and written character processing [5] to name a few. Astrophysics in particular has recently started to explore new and exciting applications of the method and its possible implications for data processing. In astronomical imaging and spectroscopy, the signal features are strictly non-negative and the constraints of the method become attractive. However, even though the *true* signal will be strictly non-negative, the *observed* data may be negative due to noise. This noise could arise from instrumental readout, from noisy calibrations, or from the subtraction of a mean value of a noisy background. Regardless of the source of the noise, it is important to note that downward fluctuations of the signal are just as valid as upward fluctuations, even when those downward fluctuations result in negative data. Any analysis of the data should treat both positive and negative values in a statistically consistent manner.

Even if all data values are positive, the noise values intrinsic in data collection mean that standard NMF as presented in (1) will perform suboptimally and will attempt to fit noise values when generating template and coefficient matrices. Prior work to handle these noise values has generally been focused on adequately weighting the fitted templates in an attempt to down weight the noisiest data, and up weight the data closest to noise-free, without concern for the negativity. This has been historically successful, with the first development along these lines being the specific NMF variant derived in [6], which uses NMF to model galaxy spectra. In this methodology, the NMF fit is weighted and the trained template vectors are constrained to be a non-negative combination of a larger set of non-negative and smooth input templates. Both the weighting of the data pixels as well as the smooth and non-negative input templates serve to prevent the algorithm from fitting the noise values of the observed data. This is ultimately a weighted version of non-negative matrix tri-factorization where one of the three matrices is initialized and held fixed through the updates. For more details on non-negative matrix tri-factorization see [7].

Other similar developments include the Heteroskedastic Matrix Factorization method in [8], which does not restrict the basis vectors to any subspace but does require them to be non-negative and weights the data. While not directly identified as a variant of NMF, the update rules presented match exactly

those of an NMF variant. A vectorized version of the same update rules was independently derived in [9]. Both of these methods were explicitly also tested on 1-dimensional galaxy spectra. The update rules presented in [9] were used for 2-dimensional galaxy images in [10] and were extended for use on larger images through the use of GPUs in [11].

An alternate and ultimately quite different development to handle the noisiness of the data is proposed in [12], where noisiness is handled by repeating a regularized but unweighted NMF fit to the noisy data many times and using a Monte Carlo analysis of these fits to determine the optimal final basis set of templates. Corresponding coefficients for the final templates are then found using a non-negative least squares solver. This too was also tested on 1-dimensional galaxy spectra.

Weighting the data pixels to account for noise is not unique to the astronomy field. [13] derived weighted update rules for NMF for analyzing gene expression data by reformulating the problem using a least squares approach. Subsequently in [14] a version of NMF is derived where the noise covariance is not diagonal (as has been assumed in the preceding papers).

One notable issue with all stated prior work in this field, however, is that standard NMF, even when weighted, does not admit **any** negativity in its data matrix \mathbf{X} . Even though weighting has shown promise in handling the noisiness of the input data, it does not explicitly handle the negative values that can be introduced by the noise. When using update rules, negative values need to be handled before fitting any templates and coefficients or else the negative values will pollute the updates and break the non-negativity constraints on \mathbf{H} and \mathbf{W} . A common handling is to clip all negative values to 0 or correspondingly set the weight of those values to 0, as is done in [6], [8]–[11], or to clip the values to some small positive value $\epsilon \lesssim 10^{-6}$ as in [12]. In high signal regimes where the signal dominates over all noise this might have only a small and perhaps unnoticeable effect. However, when we push towards low signal to noise ratio (SNR) data where the noise-free signal is extremely close to 0 and the noisiness might introduce negativity the weakness of this handling becomes evident.

A simple test elucidating the weakness of this handling is to simulate data with an expected positive signal near 0, where the noise pollutes the data with negative values. To test, we generate 500 unique instances (henceforth referred to as exposures) of a double Gaussian feature. The ratio between the heights of the two Gaussians varies between 1:2 and 2:1, with the ratio randomly chosen for each exposure. We use the noise-free true signal as the mean of a Poisson random number in each pixel to introduce Poisson noise before then adding zero-mean Gaussian noise, with independent and randomly chosen variances. We use the estimated inverse variance of each pixel as weights in the weighted NMF update rules presented in [9] where we estimate the variance by adding the variance of the Gaussian noise and the estimated variance of the signal from the Poisson process. By design the noise will drive some pixels negative outside of the Gaussian doublet. To handle this we apply the scheme where we clip all negative values to 0, as is done in the code released alongside [9]. We then generate 2 NMF templates from these 500 exposures, and attempt to

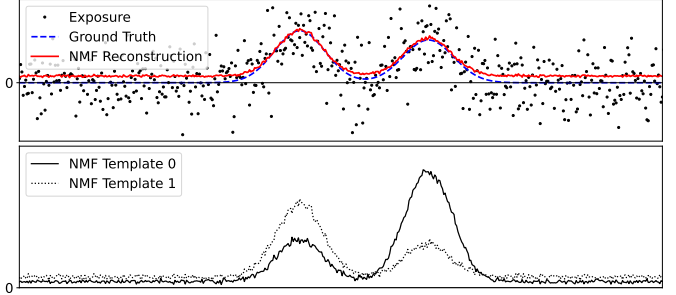


Fig. 1. Results of two weighted NMF templates generated on a toy example. See text for details of toy example. The top panel shows one representative exposure from the set of 500 as dots, with the noiseless truth and the template based reconstruction overplotted in dashed blue and solid red respectively. The bottom panel shows the two raw templates, one dotted and one solid, scaled so the maximum value is 1 but preserving the relative scale between the two templates. Notice that the templates, both the reconstruction in the upper panel and the templates themselves in the lower panel, have a positive vertical offset in the region where the truth is 0 due to the templates only fitting the positive component of the noisy data.

reconstruct the input from those two templates.

Fig. 1 shows the results of this simple test. The top panel shows a representative exposure from the data set used to generate the templates in dots, as well as the noiseless truth used to generate it (in blue and dashed) and the template based reconstruction (in red and solid). The bottom panel shows the two templates generated after 100 iterations of updates, one dotted and one solid. It is clear even in this extremely simple example that the templates introduce a positive offset from zero outside of the doublet when there is no such baseline in the true data. Since the NMF fit has only been allowed to fit the positive component of the noisy data, it has incorrectly estimated that a best fit must have a positive, non-zero, continuum in that region.

A. Our Contributions

While the standard NMF update rules cannot correctly handle negative values of the data, it is possible to consider the negative components of the data in the fit while still maintaining the non-negativity constraint on the coefficients and templates. Our contributions in this paper amount to two novel algorithms with the capability to correctly account for negative data elements caused by noise while still generating strictly non-negative coefficients and template matrices. We have named these two algorithms Shift-NMF and Nearly-NMF based on their method of fitting. Both of these algorithms additionally include weighting, which allows both algorithms to be more robust to the noise itself and to handle missing data with weights equal to 0. We will derive update rules for both of these algorithms akin to those presented in [2].

After defining the algorithms, we will demonstrate their effectiveness on the same toy problem presented in this Introduction. After validating their results on a small scale test, we will expand and validate the results with a more realistic simulated test motivated by applications to astrophysics datasets. This simulated data is designed to emulate the scale and depth of the data that these methods might realistically be

used for. This test will also motivate some brief studies of the algorithms' computational properties. Our closing remarks will summarize these results, while also presenting some possible extensions as well as potential applications of these methods to fields outside of astrophysics.

B. Notation

Throughout this paper matrices will be represented by bold uppercase letters ($\mathbf{X}, \mathbf{H}, \mathbf{W}$), vectors by lowercase bolded greek letters ($\boldsymbol{\alpha}, \boldsymbol{\beta}$) and scalars by lowercase unbolded roman letters (a, b).

The notation $\mathbf{A}_{:,i}$ will refer to the i -th column of \mathbf{A} , which is a vector. The notation $[\mathbf{A}]^+$ refers to a matrix the same shape as \mathbf{A} , where all negative values are set to zero and the positive values maintained. Correspondingly $[\mathbf{A}]^-$ is a matrix containing the absolute value of the negative elements of \mathbf{A} , with the formerly positive values set to 0, such that therefore $\mathbf{A} = [\mathbf{A}]^+ - [\mathbf{A}]^-$. $[\boldsymbol{\alpha}]^{diag}$ refers to a matrix constructed by placing the elements of the vector $\boldsymbol{\alpha}$ along the diagonal of a larger matrix.

For all following sections the open circle dot operator \circ is used for the Hadamard (elementwise) product and the division bar is applied elementwise.

II. OVERVIEW OF ALGORITHMS

A. Shift-NMF

A straightforward method to account for negative data is to use a "shift and deshift" methodology, which allows template fitting to consider the influence of normally negative values when fitting templates by shifting them to the positive half space. This is easily interpreted as a two step process:

- 1) Shift the data by a value y so that all elements are non-negative. y will depend on the input matrix, and should be equal to or larger than the most negative value in the data matrix being fit, such that the new minimum value of the dataset after the shift is ≥ 0 .
- 2) Fit the desired number of NMF templates to the shifted data with the additional fixed shift term included.

The fixing of the shift in the fitting process represents a fundamentally different solution to the NMF problem than fitting only a set of free templates to the shifted dataset. In that case, the NMF templates would fit both the data as well as the introduced offset, and would be likely also fit directly to the formerly negative values. In Shift-NMF, the shift is already accounted for in the fit, and the algorithm is only allowed to fit positive deviations away from the shift, while still accounting for the formerly negative values. The fit to the unshifted dataset is given by the fitted templates and coefficients, with the shift discarded.

To derive update rules we start by defining the shifted frame $\mathbf{X}' = \mathbf{X} + y$. The objective function to minimize, with heteroskedastic weights \mathbf{V} included, is given by

$$\chi^2 = \|\mathbf{V}^{1/2} \circ (\mathbf{X}' - \mathbf{W}\mathbf{H} - y)\|^2 \quad (3)$$

With this specification, minimizing (3) is equivalent to minimizing

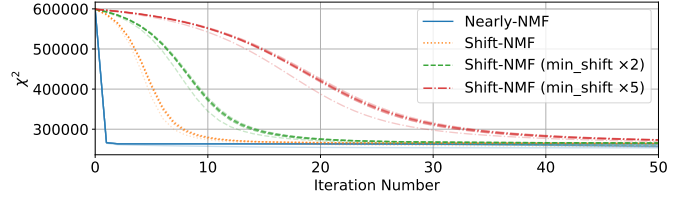


Fig. 2. Euclidean distance during training of two templates on the toy problem set out in the Introduction for the first 50 iterations, for a variety of different NMF algorithms. Nearly-NMF is plotted in solid blue, and Shift-NMF is plotted in dotted orange. In dashed green Shift-NMF was trained with a value of y that is twice the minimum shift required, and in dash-dot red y was set to five times the minimum shift. Each test was rerun 10 times with different starting points, to remove the possibility of starting point bias. It is evident that increasing the shift value beyond the minimum slows the convergence of the χ^2 value, while still training to comparable minimums given enough iterations.

$$\chi^2 = \|\mathbf{V}^{1/2} \circ (\mathbf{X} - \mathbf{W}\mathbf{H})\|^2, \quad (4)$$

the weighted but not shifted objective function.

In order to derive update rules we will take the derivative of (3) with respect to each of the two matrices to get

$$\begin{aligned} \frac{\partial \chi^2}{\partial \mathbf{H}} &= -2\mathbf{W}^T(\mathbf{V} \circ \mathbf{X}' - \mathbf{V} \circ (\mathbf{W}\mathbf{H} + y)), \\ \frac{\partial \chi^2}{\partial \mathbf{W}} &= -2(\mathbf{V} \circ \mathbf{X}' - \mathbf{V} \circ (\mathbf{W}\mathbf{H} + y))\mathbf{H}^T, \end{aligned} \quad (5)$$

and substitute them into update rules of the forms $\mathbf{H} \leftarrow \mathbf{H} - \mathbf{A}_\mathbf{H} \circ \frac{\partial \chi^2}{\partial \mathbf{H}}$, $\mathbf{W} \leftarrow \mathbf{W} - \mathbf{A}_\mathbf{W} \circ \frac{\partial \chi^2}{\partial \mathbf{W}}$, where $\mathbf{A}_\mathbf{H}$ and $\mathbf{A}_\mathbf{W}$ are learning rate hyperparameters. We can set adaptive learning rates such that

$$\begin{aligned} \mathbf{A}_\mathbf{H} &= \frac{1}{2\mathbf{W}^T(\mathbf{V} \circ (\mathbf{W}\mathbf{H} + y))} \\ \mathbf{A}_\mathbf{W} &= \frac{1}{2(\mathbf{V} \circ (\mathbf{W}\mathbf{H} + y)\mathbf{H}^T)} \end{aligned} \quad (6)$$

to derive our final multiplicative update rules:

$$\mathbf{H} \leftarrow \mathbf{H} \circ \frac{\mathbf{W}^T(\mathbf{V} \circ \mathbf{X}')}{\mathbf{W}^T(\mathbf{V} \circ (\mathbf{W}\mathbf{H} + y))} \quad (7)$$

$$\mathbf{W} \leftarrow \mathbf{W} \circ \frac{(\mathbf{V} \circ \mathbf{X}')\mathbf{H}^T}{(\mathbf{V} \circ (\mathbf{W}\mathbf{H} + y))\mathbf{H}^T} \quad (8)$$

In the limit that $y \rightarrow 0$ and therefore \mathbf{X} is entirely non-negative, so that $\mathbf{X}' = \mathbf{X}$, these two update rules correctly recover the weighted vectorized update rules derived in [9] for entirely non-negative data. A proof that these update rules monotonically decrease (3) is provided in Appendix A.

B. Nearly-NMF

The update rules presented in (7) and (8) have the caveat that the speed at which the objective χ^2 is minimized is proportional to the magnitude of the shift y , since in the limit $y \gg \mathbf{W}\mathbf{H}$, the multiplicative update factors for \mathbf{W} and \mathbf{H} asymptote to 1, i.e. larger shift values decrease the convergence rate due to smaller updates per iteration. An example of this is presented in Fig. 2, where Shift-NMF was run on the same toy dataset as before with increasingly large shift values of

twice and five times the minimum scalar shift required but with the same initial templates and coefficients. Also included on the plot is the convergence of Nearly-NMF, the derivation of which follows. Evidently, even though all three Shift-NMF algorithms are converging to the same local minimum, they are doing so at different rates dependent on the shift parameter y .

Since the rate of convergence is dependent on shift, it would therefore be most optimal to consider the smallest shift necessary. To get to the minimum possible shift we start by considering shifting each pixel in each exposure completely independently of each other, rather than shifting the entire matrix by the same scalar. This amounts to shifting such that the magnitude of each pixel's shift is equal to the pixel's value if the pixel is negative, and zero if the pixel is already positive, thus shifting only the negative pixel values by the minimum amount necessary. This promotes the shift from a scalar shift y to a shift matrix \mathbf{Y} which we can denote by $\mathbf{Y} = [\mathbf{X}]^-$ with $\mathbf{X}' = \mathbf{X} + \mathbf{Y}$, such that the objective function is

$$\chi^2 = \|\mathbf{V}^{1/2} \circ (\mathbf{X}' - \mathbf{WH} - \mathbf{Y})\|^2 \quad (9)$$

which is once again mathematically equivalent to

$$\chi^2 = \|\mathbf{V}^{1/2} \circ (\mathbf{X} - \mathbf{WH})\|^2 \quad (10)$$

and thus minimizing one is equivalent to minimizing the other. The update rules are then, following from the same math as Shift-NMF,

$$\mathbf{H} \leftarrow \mathbf{H} \circ \frac{\mathbf{W}^T(\mathbf{V} \circ \mathbf{X}')}{\mathbf{W}^T(\mathbf{V} \circ (\mathbf{WH} + \mathbf{Y}))}, \quad (11)$$

$$\mathbf{W} \leftarrow \mathbf{W} \circ \frac{(\mathbf{V} \circ \mathbf{X}')\mathbf{H}^T}{(\mathbf{V} \circ (\mathbf{WH} + \mathbf{Y}))\mathbf{H}^T}. \quad (12)$$

It follows from $\mathbf{X}' = \mathbf{X} + \mathbf{Y}$ that $\mathbf{X}' = [\mathbf{X}]^+$. Since \mathbf{V} is expected to always be positive, we can bring it inside the braces to derive the following update rules, with per pixel shifts:

$$\mathbf{H} \leftarrow \mathbf{H} \circ \frac{\mathbf{W}^T[\mathbf{V} \circ \mathbf{X}]^+}{\mathbf{W}^T(\mathbf{V} \circ (\mathbf{WH})) + [\mathbf{V} \circ \mathbf{X}]^-} \quad (13)$$

$$\mathbf{W} \leftarrow \mathbf{W} \circ \frac{[\mathbf{V} \circ \mathbf{X}]^+\mathbf{H}^T}{(\mathbf{V} \circ (\mathbf{WH}) + [\mathbf{V} \circ \mathbf{X}]^-)\mathbf{H}^T} \quad (14)$$

From here, a further optimization can be made by considering that not every pixel needs to be shifted in every iteration of updating. We will focus on \mathbf{H} for the following derivation but the same method applies to \mathbf{W} . In some cases, the negative value of the data is small enough that at some iteration the value $\mathbf{W}^T(\mathbf{V} \circ \mathbf{X}')$, is entirely non-negative, even if $(\mathbf{V} \circ \mathbf{X})$ is not. In this case the negative is already accurately accounted for in the update rule. The minimum possible shift should vary not just by pixel and exposure, but also by *iteration*. In order to derive this minimum shift we start with the elementwise inequality

$$\mathbf{W}^T(\mathbf{V} \circ (\mathbf{X}')) = \mathbf{W}^T(\mathbf{V} \circ (\mathbf{X} + \mathbf{Y})) \geq 0, \quad (15)$$

a distinctly more relaxed requirement than $\mathbf{X}' = \mathbf{X} + \mathbf{Y} \geq 0$. Importantly, any matrices that satisfy the latter inequality

also satisfy the former since \mathbf{W} and \mathbf{V} are always non-negative. Therefore this method is a further generalization of the previous method.

The minimum shift required to satisfy (15) is given by

$$\mathbf{W}^T(\mathbf{V} \circ \mathbf{Y}) = \begin{cases} \mathbf{W}^T(\mathbf{V} \circ \mathbf{X}), & \text{if } \mathbf{W}^T(\mathbf{V} \circ \mathbf{X}) < 0 \\ 0, & \text{otherwise,} \end{cases}$$

which is equivalent to

$$\mathbf{W}^T(\mathbf{V} \circ \mathbf{Y}) = [\mathbf{W}^T(\mathbf{V} \circ \mathbf{X})]^- \quad (16)$$

We can rewrite the right hand side of (11) as

$$\frac{\mathbf{W}^T(\mathbf{V} \circ \mathbf{X}')}{\mathbf{W}^T(\mathbf{V} \circ (\mathbf{WH} + \mathbf{Y}))} = \frac{\mathbf{W}^T(\mathbf{V} \circ (\mathbf{X} + \mathbf{Y}))}{\mathbf{W}^T(\mathbf{V} \circ (\mathbf{WH} + \mathbf{Y}))}, \quad (17)$$

and note that $\mathbf{W}^T(\mathbf{V} \circ \mathbf{X}) + [\mathbf{W}^T(\mathbf{V} \circ \mathbf{X})]^- = [\mathbf{W}^T(\mathbf{V} \circ \mathbf{X})]^+$ to receive our final update rules (with \mathbf{W} following from a similar procedure):

$$\mathbf{H} \leftarrow \mathbf{H} \circ \frac{[\mathbf{W}^T(\mathbf{V} \circ \mathbf{X})]^+}{\mathbf{W}^T(\mathbf{V} \circ (\mathbf{WH})) + [\mathbf{W}^T(\mathbf{V} \circ \mathbf{X})]^-} \quad (18)$$

$$\mathbf{W} \leftarrow \mathbf{W} \circ \frac{[(\mathbf{V} \circ \mathbf{X})\mathbf{H}^T]^+}{(\mathbf{V} \circ (\mathbf{WH}))\mathbf{H}^T + [(\mathbf{V} \circ \mathbf{X})\mathbf{H}^T]} \quad (19)$$

An important last part of the derivation is to underscore that in general $[\mathbf{W}^T(\mathbf{V} \circ \mathbf{X})]^+ \neq \mathbf{W}^T[(\mathbf{V} \circ \mathbf{X})]^+$, and correspondingly for the other splits, meaning that these update rules are distinct from those in (13) and (14).

We call this method Nearly-NMF, as it is “nearly” non-negative, in that it keeps the non-negative constraints on \mathbf{W} and \mathbf{H} , while removing the non-negative constraint on the data \mathbf{X} . In the limit where \mathbf{X} contains no negative elements, the two terms $[\mathbf{W}^T(\mathbf{V} \circ \mathbf{X})]^+$ and $[(\mathbf{V} \circ \mathbf{X})\mathbf{H}^T]^+$ will go to zero, with $[\mathbf{W}^T(\mathbf{V} \circ \mathbf{X})]^+ \rightarrow \mathbf{W}^T(\mathbf{V} \circ \mathbf{X})$ and $[(\mathbf{V} \circ \mathbf{X})\mathbf{H}^T]^+ \rightarrow (\mathbf{V} \circ \mathbf{X})\mathbf{H}^T$, once again correctly recovering the original weighted update rules presented in [9]. A proof that these update rules monotonically decrease the χ^2 in (10) with the given constraints is provided in Appendix B.

III. NUMERICAL EXAMPLES

A. Toy Problem

As a first test that Shift-NMF and Nearly-NMF correctly handle the negative noise, we will return to the toy problem set up in the Introduction. Using the same dataset, the results of running Shift-NMF and Nearly-NMF are plotted in Fig. 3. Both Shift-NMF and Nearly-NMF correctly generate templates that account for the negative components of the noise, and do not present the positive offset that weighted or standard NMF does.

B. Simulated Data

For a more realistic example, we turn to an astronomy-motivated case — building NMF templates to model quasar spectra (flux vs. wavelength of light). Quasars are among the brightest objects in the universe, visible to billions of light-years away using large modern research telescopes. As the

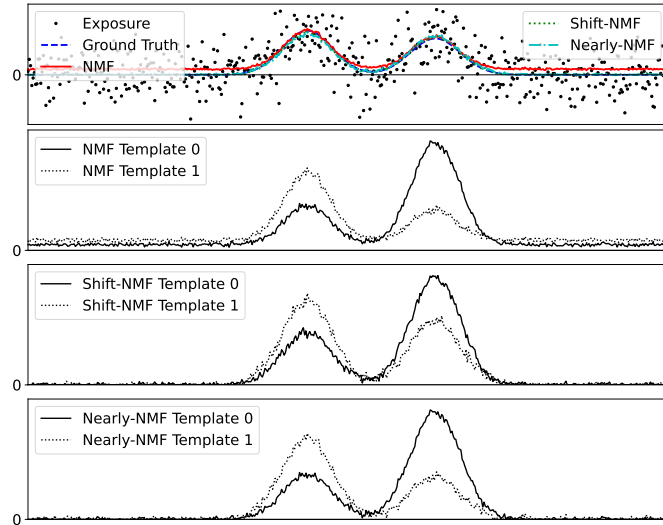


Fig. 3. Results of two NMF templates generated on a toy example, for each of the three algorithms: regular weighted NMF, Shift-NMF, and Nearly-NMF. See Introduction for details of toy example. Top panel shows one representative exposure from the set of 500 in dots, with the noiseless truth and the template based reconstructions overplotted in varying styles. Note that the reconstructions from two methods presented in this paper, Shift-NMF and Nearly-NMF, are nearly indistinguishable from the truth, and lie directly on top of it. The next three panels shows the two raw templates, scaled so the maximum value is 1 but preserving the relative scale between the two templates. Shift-NMF and Nearly-NMF templates correctly go to zero on the edges, whereas weighted NMF has a vertical offset

light travels from the quasar to earth, the expansion of the universe causes a multiplicative shift in the wavelengths of the light by a factor of $(1 + z)$ where z is the “redshift” of the quasar. More distant quasars have larger redshifts due to the light experiencing more expansion of the universe between the time it leaves the quasar and when it arrives at earth. Templates of quasar spectra are used to model newly observed spectra to confirm their identification and measure their redshift. [15] used 568 quasar spectra to build Principal Component Analysis (PCA) templates for the Baryon Oscillation Spectroscopic Survey (BOSS); [16] used a much larger set of 207 956 quasar spectra from the extended Baryon Oscillation Spectroscopic Survey (eBOSS) [17] to build new PCA templates for the Dark Energy Spectroscopic Survey [18], [19]. Although PCA algorithms such as EMPCA [20] (used by [16]) and [21] accommodate noisy, negative, and missing data, a downside of PCA templates is that they can be overly flexible in overfitting noise, since they don’t have the constraint that the true underlying signal is strictly positive. NMF templates could provide improved results by eliminating a class of unphysical false positives in the fits of templates to data.

To have a ground truth for comparison in this study, we used simqso [22] to generate 200 000 simulated quasar spectra with random uniform redshifts between 0 and 4. We use 130 000 of these spectra as a training sample, and hold out the remaining 70 000 as a validation sample. The generated spectra have logarithmically spaced wavelengths λ from 360–1000 nm with a spacing of $\Delta \log \lambda = 10^{-4}$, approximately matching the wavelength coverage of the BOSS quasar sample [23]. In order

to simulate Poisson statistics we convert the simulated flux to a photon estimate and use the scaled noiseless value in each wavelength bin as the mean for a random Poisson draw. We use that Poisson value as the spectral value for that wavelength. We add zero-mean Gaussian noise to these resultant spectra, such that the expected average SNR of the Gaussian noise is around 1.5.¹

Observed spectra cover a fixed wavelength range in the “observer-frame”, however, due to the redshift effect these correspond to a different wavelength range per quasar in their source “rest-frame”. Thus building an NMF model that covers all wavelengths is not just a noisy-data problem, but also a missing-data problem since no individual spectrum covers all wavelengths of interest. To build templates, we de-redshift all simulated quasars onto common wavelength grid in their rest-frame, using weights of 0 for any missing data due to any wavelengths that cannot be measured in the observer-frame. This produces an input dimensionality, d , of 11 400 pixels spanning all wavelengths. Finally, we re-normalize the median flux of each quasar to match the median flux over the same rest-frame wavelength range of a common reference quasar so that variations are due to spectral diversity rather than overall amplitude fluctuations. We also correspondingly rescale the variance.

An example of this process is shown in Fig. 4. In the upper panel are three simulated quasars in the observed frame, with the noise-free truth plotted over the noisy simulated exposure. In the bottom panel these quasars are shown in the rest-frame, plotted on the common wavelength grid. It is evident that none of the individual quasar spectra cover the entire wavelength range to be modeled, and every wavelength is only covered by a subset of the input training spectra, with no individual pixel covered by every spectra. Before fitting the templates, we trim the common wavelength grid to avoid edge effects due to low numbers of quasars in edge pixels. We trim 50 pixels off the low end, and 300 pixels off the high end, to fit a total range of 11 050 pixels. This presents a realistically challenging dataset for NMF modeling, including 61.1% of data being “missing,” 11.4% of non-missing data being negative (due to noisy “observations” of an underlying strictly positive signal), variable noise, and a $11\,050 \times 130\,000$ dataset to solve for a set of NMF templates modeling all wavelengths.

For this simulated test we focused on Nearly-NMF due to its faster convergence than Shift-NMF, and generated 5 templates on both the noisy datasets as well as the noise-free, true, underlying spectra. We will use the templates generated on the true spectra to validate how well the algorithm handles both the noise and the introduced negativity. In order to generate templates ordered such that subsequent templates approximately explain less variance than the previous template, similar to that of PCA, we generate the templates sequentially. The sequential NMF method is detailed further in [9] and [10], but we will provide a summary. We start by generating one template from a linear starting point with random uniform coefficients for

¹Real astronomical spectra have an even more complex noise model due to wavelength-dependent instrument throughput and backgrounds, but the level of complexity used in the simulated data for this study is sufficient to demonstrate the performance of the Shift- and Nearly-NMF methods.

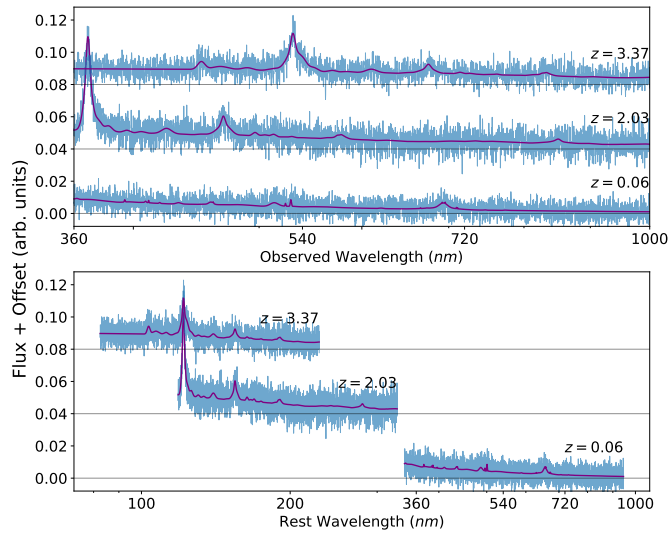


Fig. 4. An example of the process used to generate the quasar dataset. In both panels three unnormalized spectra are offset vertically from each other by a constant value 0.04. In the upper panel, three different noisy spectra are plotted in light blue in the observed frame, as the simulated instrument would record them, with their noise-free base spectra overplotted in purple. The three spectra are annotated by their redshift value at the far right of the plot. Note in the noisy data the high prevalence of negative values due to the noise. In the lower panel we demonstrate the spectra as they are used in both Shift-NMF and Nearly-NMF, now in the rest frame. It is evident that the spectra cover different amounts of the wavelength grid, with none of them covering the entirety of the fitting space. The spectra plotted here are not renormalized, which is done before fitting.

each exposure. After that template is trained for a smaller number of iterations (~ 50) we stop and train two templates, with the first template initialized to the previously trained template and the new template initialized to a linear start, with a corresponding trained coefficient and random coefficient respectively for this set of templates. We do not hold the previously trained template fixed, allowing it to continue to be trained. We repeat this sequential method until we have 5 templates. The 5 templates are then refined through an additional 1000 iterations of updates. The final number of iterations, 1000, is chosen to ensure convergence to a local minima template. The final Nearly-NMF templates generated in this test are shown in Fig. 5. All templates are plotted in the order they were generated in the sequential methodology explained prior.

For all cases it can be seen that Nearly-NMF has correctly accounted for the noise in the input spectra, and has recovered templates that incorporate many of the same details that the noise-free templates capture. Both sets of templates are also correctly non-negative, and feature no negative values. Nearly-NMF has correctly accounted for the zero-mean property of the noise and has produced templates that appear similarly close to zero as the noise-free templates.

The increased noise in the noisy templates in the low wavelength and high wavelength regions are to be expected. Due to the non-linear nature of de-redshifting spectra, the number of spectra and the corresponding summed weight in each pixel is not uniform. A plot of the summed weight in each pixel is shown in the top panel of Fig. 5, where it is

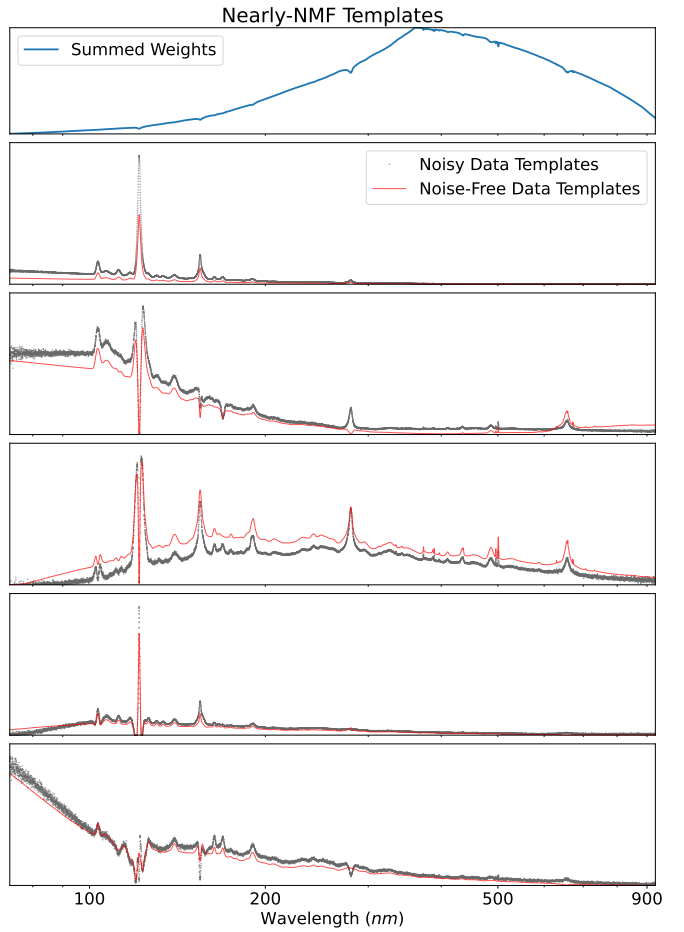


Fig. 5. The top panel shows the sum of the inverse variance weights in each pixel over the wavelength region covered by the templates. The next 5 panels show each of the 5 NMF templates, generated on both the noisy and noise-free datasets. The noise-free templates are plotted as a solid line in red, while the noisy templates are dotted in light gray. Templates are plotted on their logarithmic grid, with a logarithmic scaling on the x-axis. The noisy templates have still recovered most of the same features present in the noise-free templates, and have good agreement even though the noisy data has a significant amount of negative values. The regions where the templates are noisiest correspond with the same regions where the sum of the weights is low.

evident that the noisier regions of the templates correspond with lower total summed weight in that pixel.

In order to validate that the templates generated on the noisy dataset are comparably good to the templates generated on the noise-free truth dataset, we fit both sets of templates to the holdout 70 000 validation dataset of quasars. For this test we use a non-negative least squares solver provided by `scipy` [24] to find coefficients for each template to remove the impact of picking a bad starting point for the fit. Once we fit both sets of templates to the validation dataset, we calculate their χ^2 values using (10), and then make a histogram of the difference between the noise-free and noisy fits. These results are shown in Fig. 6. A vertical line denotes the median difference between the noise-free and noisy fits, at about 0.486, in comparison to the typical absolute $\chi^2 \sim 4440$. The slight positive shift of the data indicates that the noisy templates fit the data slightly worse than the noise-free templates, but

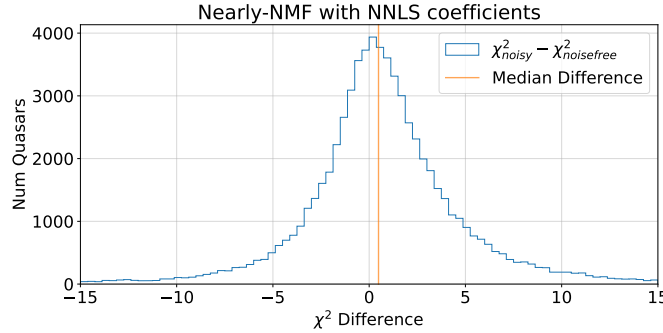


Fig. 6. Comparison between the χ^2 values from fitting the 70 000 validation dataset by both the noisy and noise-free templates. A vertical line at about 0.486 indicates the median difference, compared to the typical absolute $\chi^2 \sim 4440$. A small positive offset means that the noisy templates fit the data slightly worse, but its proximity to zero indicates that they are comparably good fits.

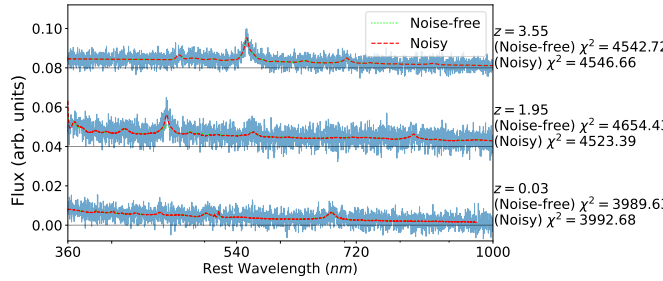


Fig. 7. Three quasars from the noisy validation set plotted in the observed frame with their Nearly-NMF reconstructions overplotted, with the reconstruction from the noise-free templates in dot dash green and the reconstruction from the noisy templates in dashed red. Both reconstructions are comparable and nearly identical, validated by their similar Euclidean distances from the data, annotated at right. It is notable that the two reconstructions, despite one being derived from templates trained on noisy data, are remarkably similar. Note also some missing pixels in the reconstruction of the bottom spectra, due to the clipping of the fitting region to avoid edge effects. In this plot we are plotting the non-renormalized spectra, as in Fig. 4, with the reconstructions rescaled to match.

the remarkably sharp peak near 0 indicates that even though one set of templates are generated on noisy data with a non-trivial amount of negative values, they are fitting the dataset comparably well as templates generated on the underlying noise-free truth, which has no noise and is entirely non-negative.

An example of how closely matched these reconstructions between that of the noisy and noise-free templates is given in Fig. 7. Plotted in the figure are three quasars of similar redshift to those plotted in Fig. 4, however these quasars are drawn from the validation set and were not included in training. Their fits from the noise-free and noisy templates are both overplotted, and are similar to each other.

IV. COMPUTATIONAL PROPERTIES OF THE ALGORITHMS

In this section we will investigate some basic computational properties of the Nearly-NMF algorithm. In theory we would expect both algorithms to scale, in big- O notation, roughly in terms of $O(n \times d \times q \times n_{iter})$, where n, d, q are the variables set out in the Introduction, and n_{iter} is the chosen number of iterations to run the update rules. To test this we set up

individual parameter sweeps for the three values of interest (n, d, q) and time the amount of time it takes to do one single iteration of both \mathbf{H} and \mathbf{W} Nearly-NMF update rules. Each test is run for 100 iterations, and we plot the median values of these 100 runs with error bars equal to the standard deviation of the runs. For these timing runs we force the algorithm to use only a single thread but some speedup, especially at higher values of d and n , can be achieved by allowing it to use more threads. Additionally, although we implemented and used a GPU version of both algorithms for generating the templates in Fig. 5, we used the CPU implementation for the following timing tests. These tests were run on a dual AMD EPYC 7763 CPU system with 512 GB of RAM, corresponding to a single node on the National Energy Research Scientific Computing Center’s (NERSC) Perlmutter system. The results of the timing runs are included in Fig. 8. Specific details for each metric’s timing runs are as follows:

- For n , we train 5 templates, and use half of the original dimensionality of the dataset presented in this paper ($d = 5700$). We take a logarithmically spaced number quasars from 50 up to 2000, and at each point use a randomly selected subsample of the quasar superset generated for this paper.
- For q we use a fixed value of 750 quasars, and half of the original dimensionality of the dataset presented in this paper. We vary the number of templates trained from 1 up to 10.
- For d we use a fixed value of 750 quasars and train 5 templates. We rebin the input dataset from the original to varying sizes such that each subsequent rebinning is half the dimensionality of the previous.

We have also confirmed that the scaling relations hold true for Shift-NMF, with per-iteration timings similar to those reported for Nearly-NMF in Fig. 8, with the same scaling relations, but do not explicitly plot them. As expected for all three variables, the scaling relations are approximately linear.

V. CONCLUSION

In this paper we have presented two new versions of non-negative matrix factorization, Shift-NMF and Nearly-NMF, that can adequately handle noisy data with negative values introduced by noise while still obeying the non-negativity constraint on the coefficients and templates. Both of these algorithms are robust to the noise as well as missing data and have straightforward update rules akin to those of [2]. We have also shown that in a realistic test with large amounts of missing and negative data that Nearly-NMF can recover templates giving equally as good fits as templates generated on the noise-free truth.

Both of these methods were developed in an astronomical context, but their applications are not limited to only this regime. Non-negative matrix factorization has been applied to a variety of other fields where negative data can arise either naturally in the data or as part of a data processing step. Some examples include [25] for NMR spectroscopy, [26] for brain pattern analysis in neuroscience or [27] for bioinformatics. All of these fields might benefit from NMF style algorithms that

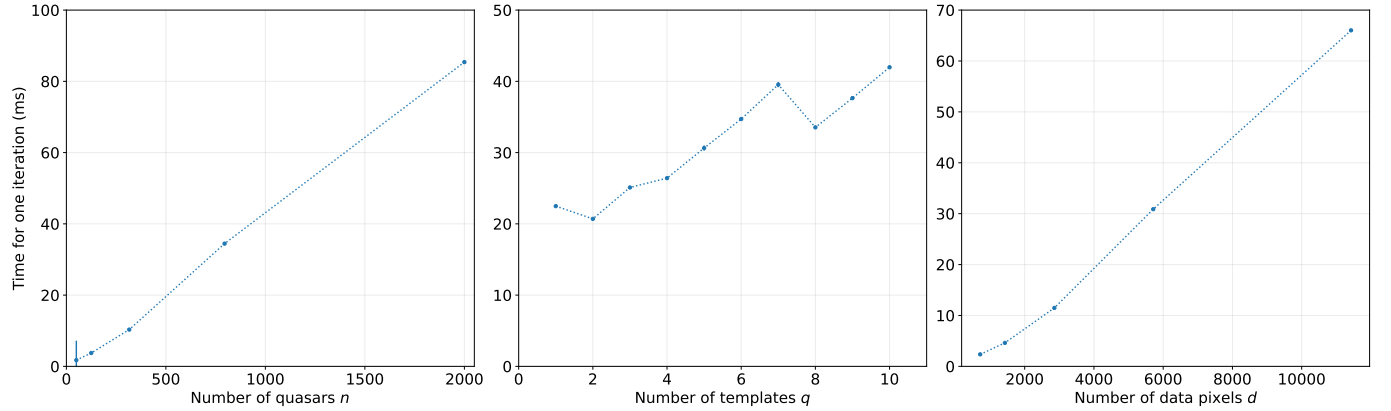


Fig. 8. Results of three different timing runs for Nearly-NMF. In each plot we hold the other two variables fixed. The fixed values for the variables not varying in each plot are $N = 750$, $q = 5$ and $d = 5700$. Each point is the median time to complete a single iteration of updates, taken from 100 subsequent iterations. Error bars are plotted as the standard deviation of these 100 iterations. Note that in almost all cases the error bars are smaller than the point size, representing considerable stability in timing.

can handle some negative values in the input data, when the negative data is expected to result from zero-mean noise.

We release our implementations of the Shift-NMF and Nearly-NMF algorithms for public use at https://github.com/dylanagreen/nearly_nmf. This code is written in Python, is optimized for both CPU use through numpy [28], and GPU use through cupy [29], and was used to train the templates plotted in this paper. Included within the linked repository is all code necessary to reproduce the plots and analysis in this paper.

APPENDIX

This appendix includes proofs that the update rules provided in the main text of the paper monotonically decrease their respective χ^2 objectives.

A. Shift-NMF

To prove the Shift-NMF update rules monotonically decrease their χ^2 objective we will start with \mathbf{H} . We can rewrite (7) in column-wise form as

$$\mathbf{H}_{:,i} \leftarrow \mathbf{H}_{:,i} \circ \frac{\mathbf{W}^T(\mathbf{V}_{:,i} \circ \mathbf{X}'_{:,i})}{\mathbf{W}^T(\mathbf{V}_{:,i} \circ (\mathbf{W}\mathbf{H}_{:,i} + y))}, \quad (20)$$

and then use the following transforms that mirror those from [9]:

$$\hat{\mathbf{X}}_{:,i} = \mathbf{V}_{:,i} \circ \mathbf{X}'_{:,i}, \quad (21)$$

$$\hat{\mathbf{W}} = [\mathbf{V}_{:,i}]^{diag} \mathbf{W}, \quad (22)$$

$$\hat{\Phi}_{:,i} = y \mathbf{V}_{:,i}, \quad (23)$$

to rewrite (20) as

$$\mathbf{H}_{:,i} \leftarrow \mathbf{H}_{:,i} \circ \frac{\mathbf{W}^T(\hat{\mathbf{X}}_{:,i})}{\mathbf{W}^T((\hat{\mathbf{W}}\mathbf{H}_{:,i} + \hat{\Phi}_{:,i})}. \quad (24)$$

This equation matches the form of (41) in [30], which is already proven to monotonically decrease the objective function. Therefore our update rule in (7) follows the same conclusion. A similar breakdown of the objective function

relative to the rows of \mathbf{W} can be worked through, and the same proof from [30] can be applied to prove the same result for (8).

B. Nearly-NMF

In order to prove that χ^2 is non-increasing under the update rules (18) and (19) we will construct auxiliary functions, F , and prove that the update rules are global minima of the auxiliary functions. Auxiliary functions fulfill two properties:

$$F(\mathbf{A}, \tilde{\mathbf{A}}) \geq \chi^2(\mathbf{A}), F(\mathbf{A}, \mathbf{A}) = \chi^2(\mathbf{A}), \quad (25)$$

for any matrix \mathbf{A} and $\tilde{\mathbf{A}}$ where for our case \mathbf{A} is either \mathbf{W} or \mathbf{H} . For simplicity we will construct this proof on the unweighted case, and then show that under a simple transform, as in Section A, the weighted case fulfills the same proof. To start, it is useful to rewrite the unweighted objective $\chi^2 = \|\mathbf{X} - \mathbf{WH}\|^2$ (from (10)) in scalar form as

$$\begin{aligned} \chi^2 = \sum_i \Big(& -2 \left(\sum_{jk} [\mathbf{X}_{ji} \mathbf{W}_{jk}]^+ \mathbf{H}_{ki} \right) \\ & + 2 \left(\sum_{jk} [\mathbf{X}_{ji} \mathbf{W}_{jk}]^- \mathbf{H}_{ki} \right) \\ & + \sum_{jkl} \mathbf{H}_{ji} \mathbf{W}_{jk} \mathbf{W}_{kl} \mathbf{H}_{li} \Big), \end{aligned} \quad (26)$$

where it is important to note that we have dropped the term $\sum_{ij} \mathbf{X}_{ji} \mathbf{X}_{ji}$ since minimizing χ^2 with respect to either \mathbf{H} or \mathbf{W} is independent of this term. Using the fact that for any scalar $a, b > 0$, $a \leq (a^2 + b^2)/2b$ from [31], and for any non-negative vectors $\boldsymbol{\alpha}, \boldsymbol{\beta}$ and non-negative matrix \mathbf{P} , $\sum_{ij} \boldsymbol{\alpha}_i \boldsymbol{\alpha}_j \mathbf{P}_{ij} \leq \sum_{ij} \boldsymbol{\alpha}_i^2 \frac{\boldsymbol{\beta}_j}{\boldsymbol{\beta}_i} \mathbf{P}_{ij}$ from [6], we will construct

the function

$$\begin{aligned} F(\mathbf{H}, \tilde{\mathbf{H}}) = & -2 \sum_{ijk} [\mathbf{X}_{ji} \mathbf{W}_{jk}]^+ \mathbf{H}_{ki} \\ & + \sum_{ijk} [\mathbf{X}_{ji} \mathbf{W}_{jk}]^- \frac{\mathbf{H}_{ki}^2 + \tilde{\mathbf{H}}_{ki}^2}{\tilde{\mathbf{H}}_{ki}} \\ & + \sum_{ijkl} \mathbf{W}_{kj} \mathbf{W}_{kl} \mathbf{H}_{li}^2 \frac{\tilde{\mathbf{H}}_{ji}}{\tilde{\mathbf{H}}_{li}} \end{aligned} \quad (27)$$

This function fulfills the criteria $F(\mathbf{H}, \mathbf{H}) = \chi^2(\mathbf{H})$, and given the above two properties it also follows that $F(\mathbf{H}, \tilde{\mathbf{H}}) \geq \chi^2(\mathbf{H})$ holds for any arbitrary $\mathbf{H} \geq 0$ and $\tilde{\mathbf{H}} \geq 0$. Next we will prove that $F(\mathbf{H}, \tilde{\mathbf{H}})$ is convex. Proving the convexity of $F(\mathbf{H}, \tilde{\mathbf{H}})$ necessitates the second derivative, allowing us to compute the first derivative along the way:

$$\begin{aligned} \frac{\partial F(\mathbf{H}, \tilde{\mathbf{H}})}{\partial \mathbf{H}_{ab}} = & -2 \sum_j [\mathbf{X}_{jb} \mathbf{W}_{ja}]^+ \\ & + 2 \sum_j [\mathbf{X}_{jb} \mathbf{W}_{ja}]^- \frac{\mathbf{H}_{ab}}{\tilde{\mathbf{H}}_{ab}} \\ & + 2 \sum_{jk} \mathbf{W}_{kj} \mathbf{W}_{ka} \mathbf{H}_{ab} \frac{\tilde{\mathbf{H}}_{jb}}{\tilde{\mathbf{H}}_{ab}} \end{aligned} \quad (28)$$

$$\begin{aligned} \frac{\partial^2 F(\mathbf{H}, \tilde{\mathbf{H}})}{\partial \mathbf{H}_{ab} \partial \mathbf{H}_{cd}} = & 2\delta_{ac}\delta_{bd} \left(\sum_j \frac{[\mathbf{X}_{jb} \mathbf{W}_{ja}]^-}{\tilde{\mathbf{H}}_{ab}} \right. \\ & \left. + \sum_{jk} \mathbf{W}_{kj} \mathbf{W}_{ka} \frac{\tilde{\mathbf{H}}_{jb}}{\tilde{\mathbf{H}}_{ab}} \right), \end{aligned} \quad (29)$$

where δ_{ij} is the Kronecker delta for indices i and j .

Equation (29) is a diagonal matrix with strictly positive elements on the diagonal given the constraints and is therefore positive semidefinite. From this it follows that $F(\mathbf{H}, \tilde{\mathbf{H}})$ is a convex function, with a global minimum found by setting (28) equal to 0. Following this procedure and rearranging we get that $\frac{\partial F(\mathbf{H}, \tilde{\mathbf{H}})}{\partial \mathbf{H}_{ab}} = 0$ when

$$\mathbf{H}_{ab} = \tilde{\mathbf{H}}_{ab} \frac{\sum_j [\mathbf{X}_{jb} \mathbf{W}_{ja}]^+}{\sum_j [\mathbf{X}_{jb} \mathbf{W}_{ja}]^- + \sum_{jk} \mathbf{W}_{kj} \mathbf{W}_{ka} \tilde{\mathbf{H}}_{jb}}. \quad (30)$$

Setting $\tilde{\mathbf{H}} = \mathbf{H}$ such that $F(\mathbf{H}, \tilde{\mathbf{H}}) = \chi^2(\mathbf{H})$, from (25), this is exactly the update rule presented in (18) without weights, thus proving that in the unweighted case the Nearly-NMF update rule monotonically decreases χ^2 with each iteration. The weighted case proof follows from using the diagonalized version of the per exposure weights, $[\mathbf{V}_{,i}]^{diag}$, such that the scalar objective in (26) becomes

$$\begin{aligned} \chi^2 = & -2 \sum_{ijk} [([\mathbf{V}_{,i}]^{diag} \mathbf{X})_{ji} ([\mathbf{V}_{,i}]^{diag} \mathbf{W})_{jk}]^+ \mathbf{H}_{ki} \\ & + \sum_{ijk} [([\mathbf{V}_{,i}]^{diag} \mathbf{X})_{ji} ([\mathbf{V}_{,i}]^{diag} \mathbf{W})_{jk}]^- \mathbf{H}_{ki} \\ & + \sum_{ijkl} ([\mathbf{V}_{,i}]^{diag} \mathbf{W})_{kj} ([\mathbf{V}_{,i}]^{diag} \mathbf{W})_{kl} \mathbf{H}_{li} \mathbf{H}_{ji} \end{aligned} \quad (31)$$

We can use the same transform as Appendix A,

$$\hat{\mathbf{X}}_{,i} = [\mathbf{V}_{,i}]^{diag} \mathbf{X}_{,i}, \quad (32)$$

$$\hat{\mathbf{W}} = [\mathbf{V}_{,i}]^{diag} \mathbf{W}, \quad (33)$$

to recover the same form as (26). The only difference is that in this version the value of $\hat{\mathbf{W}}$ will depend on the index i . However, this index will become fixed under the derivative with respect to \mathbf{H}_{ab} in (28) by the delta function δ_{ib} , and the proof proceeds the same way without any further alteration and eventually recovering a weighted version of (30), and therefore a scalar summation form of (18). This completes the proof for the \mathbf{H} update rule.

The proof for the \mathbf{W} update rule given in (19) follows the same steps, both the weighted and unweighted case. Since the outline is the same, it is not necessary to present the entirety of the steps except to note that the auxiliary function is now

$$\begin{aligned} F(\mathbf{W}, \tilde{\mathbf{W}}) = & -2 \sum_{ijk} [\mathbf{X}_{ji} \mathbf{H}_{ki}]^+ \mathbf{W}_{jk} \\ & + \sum_{ijk} [\mathbf{X}_{ji} \mathbf{H}_{ki}]^- \frac{\mathbf{W}_{jk}^2 + \tilde{\mathbf{W}}_{jk}^2}{\tilde{\mathbf{W}}_{jk}^2} \\ & + \sum_{ijkl} \mathbf{H}_{ji} \mathbf{W}_{kj}^2 \frac{\tilde{\mathbf{W}}_{kl}}{\tilde{\mathbf{W}}_{kj}} \mathbf{H}_{li}. \end{aligned} \quad (34)$$

ACKNOWLEDGMENTS

The authors would like to thank Dr. D. Kirkby and M. Dowicz for their valuable discussion and input.

REFERENCES

- [1] P. Paatero and U. Tapper, “Positive matrix factorization: A non-negative factor model with optimal utilization of error estimates of data values,” *Environmetrics*, vol. 5, no. 2, pp. 111–126, 1994.
- [2] D. Lee and H. S. Seung, “Algorithms for Non-negative Matrix Factorization,” in *Advances in Neural Information Processing Systems*, vol. 13. MIT Press, 2000.
- [3] V. P. Pauca, J. Piper, and R. J. Plemmons, “Nonnegative matrix factorization for spectral data analysis,” *Linear Algebra and its Applications*, vol. 416, no. 1, pp. 29–47, Jul. 2006.
- [4] Y. Li and A. Ngom, “The non-negative matrix factorization toolbox for biological data mining,” *Source Code for Biology and Medicine*, vol. 8, no. 1, p. 10, Apr. 2013.
- [5] C.-Y. Lin, L.-W. Kang, T.-Y. Huang, and M.-K. Chang, “A novel non-negative matrix factorization technique for decomposition of Chinese characters with application to secret sharing,” *EURASIP Journal on Advances in Signal Processing*, vol. 2019, no. 1, p. 35, Aug. 2019.
- [6] M. R. Blanton and S. Roweis, “ K -Corrections and Filter Transformations in the Ultraviolet, Optical, and Near-Infrared,” *The Astronomical Journal*, vol. 133, no. 2, pp. 734–754, Feb. 2007.
- [7] A. Čopar, B. Zupan, and M. Zitnik, “Fast optimization of non-negative matrix tri-factorization,” *PLOS ONE*, vol. 14, no. 6, p. e0217994, Jun. 2019, publisher: Public Library of Science.
- [8] P. Tsalmantza and D. W. Hogg, “A Data-driven Model for Spectra: Finding Double Redshifts in the Sloan Digital Sky Survey,” *The Astrophysical Journal*, vol. 753, p. 122, Jul. 2012.
- [9] G. Zhu, “Nonnegative Matrix Factorization (NMF) with Heteroscedastic Uncertainties and Missing data,” *arXiv:1612.06037*, Dec. 2016.
- [10] B. Ren, L. Pueyo, G. B. Zhu, J. Debes, and G. Duchêne, “Non-negative Matrix Factorization: Robust Extraction of Extended Structures,” *The Astrophysical Journal*, vol. 852, no. 2, p. 104, Jan. 2018, publisher: The American Astronomical Society.
- [11] S. K. P. M. et al., “NMF-based GPU accelerated coronagraphy pipeline,” in *Techniques and Instrumentation for Detection of Exoplanets XI*, G. J. Ruane, Ed., vol. 12680, International Society for Optics and Photonics. SPIE, 2023, p. 1268021.
- [12] A. Boulais, O. Berné, G. Faury, and Y. Deville, “Unmixing methods based on nonnegativity and weakly mixed pixels for astronomical hyperspectral datasets,” *Astronomy & Astrophysics*, vol. 647, p. A105, Mar. 2021.
- [13] G. Wang, A. V. Kossenkov, and M. F. Ochs, “LS-NMF: A modified non-negative matrix factorization algorithm utilizing uncertainty estimates,” *BMC Bioinformatics*, vol. 7, no. 1, p. 175, Mar. 2006.

- [14] S. M. Plis, V. K. Potluru, V. D. Calhoun, and T. Lane, “Correlated noise: How it breaks NMF, and what to do about it,” in *2009 IEEE International Workshop on Machine Learning for Signal Processing*, Sep. 2009, pp. 1–6.
- [15] A. S. Bolton *et al.*, “Spectral Classification and Redshift Measurement for the SDSS-III Baryon Oscillation Spectroscopic Survey,” *The Astronomical Journal*, vol. 144, no. 5, p. 144, Nov. 2012.
- [16] A. Brodzeller *et al.*, “Performance of the Quasar Spectral Templates for the Dark Energy Spectroscopic Instrument,” *The Astronomical Journal*, vol. 166, no. 2, p. 66, Aug. 2023.
- [17] B. W. Lyke *et al.*, “The Sloan Digital Sky Survey Quasar Catalog: Sixteenth Data Release,” *The Astrophysical Journal Supplement Series*, vol. 250, no. 1, p. 8, Sep. 2020.
- [18] DESI Collaboration *et al.*, “Validation of the Scientific Program for the Dark Energy Spectroscopic Instrument,” *arXiv:2306.06307*, Jun. 2023.
- [19] J. Guy *et al.*, “The Spectroscopic Data Processing Pipeline for the Dark Energy Spectroscopic Instrument,” *The Astronomical Journal*, vol. 165, no. 4, p. 144, Apr. 2023.
- [20] S. Bailey, “Principal Component Analysis with Noisy and/or Missing Data,” *Publications of the Astronomical Society of the Pacific*, vol. 124, pp. 1015–1023, Sep. 2012.
- [21] L. Delchambre, “Weighted principal component analysis: a weighted covariance eigendecomposition approach,” *Monthly Notices of the Royal Astronomical Society*, vol. 446, no. 4, pp. 3545–3555, Feb. 2015.
- [22] I. McGreer, J. Moustakas, and J. Schindler, “simqs: Simulated quasar spectra generator,” Astrophysics Source Code Library, record ascl:2106.008, Jun. 2021.
- [23] K. S. Dawson *et al.*, “The SDSS-IV Extended Baryon Oscillation Spectroscopic Survey: Overview and Early Data,” *The Astronomical Journal*, vol. 151, no. 2, p. 44, Feb. 2016.
- [24] P. Virtanen *et al.*, “SciPy 1.0: Fundamental Algorithms for Scientific Computing in Python,” *Nature Methods*, vol. 17, pp. 261–272, 2020.
- [25] R. J. McCarty, N. Ronghe, M. Woo, and T. M. Alam, “Blind Source Separation for NMR Spectra with Negative Intensity,” *arXiv:2002.03009*, Feb. 2020.
- [26] “Chapter 16 - Time-Frequency Methodologies in Neurosciences,” in *Time-Frequency Signal Analysis and Processing (Second Edition)*, second edition ed., B. Boashash, Ed. Oxford: Academic Press, 2016, pp. 915–966.
- [27] P. M. Kim and B. Tidor, “Subsystem Identification Through Dimensionality Reduction of Large-Scale Gene Expression Data,” *Genome Research*, vol. 13, no. 7, pp. 1706–1718, Jul. 2003.
- [28] C. R. Harris *et al.*, “Array programming with NumPy,” *Nature*, vol. 585, no. 7825, pp. 357–362, Sep. 2020.
- [29] R. Okuta, Y. Unno, D. Nishino, S. Hido, and C. Loomis, “Cupy: A numpy-compatible library for nvidia gpu calculations,” in *Proceedings of Workshop on Machine Learning Systems (LearningSys) in The Thirty-first Annual Conference on Neural Information Processing Systems (NIPS)*, 2017.
- [30] W. Tang, Z. Shi, and Z. An, “Nonnegative matrix factorization for hyperspectral unmixing using prior knowledge of spectral signatures,” *Optical Engineering*, vol. 51, no. 8, p. 087001, Aug. 2012.
- [31] C. H. Ding, T. Li, and M. I. Jordan, “Convex and Semi-Nonnegative Matrix Factorizations,” *IEEE Transactions on Pattern Analysis and Machine Intelligence*, vol. 32, no. 1, pp. 45–55, Jan. 2010.

Dylan Green received his B.S., and is currently a Ph.D. candidate, in Physics at the University of California, Irvine, in the Department of Physics and Astronomy. He is a member of the Dark Energy Spectroscopic Instrument, and his research interests include using physics first principles to improve data processing for cosmology.



Stephen Bailey is a senior software developer in the Physics Division at Lawrence Berkeley National Lab. He has been working with large data modeling for over 3 decades, starting with writing a matchmaking app for his high school. Along the way he earned a B.S. degree in Physics from the University of Washington and a Ph.D. in Physics from Harvard University. He currently leads the Data Management team for the Dark Energy Spectroscopic Instrument, where he enjoys processing raw data into useful data to study cosmology.

